Capillary oscillations of a constrained liquid drop

J. B. Bostwick[1,a)] and P. H. Steen[2,b)]
[1]*Department of Theoretical and Applied Mechanics, Cornell University, Ithaca, New York 14853, USA*
[2]*School of Chemical and Biomolecular Engineering and Center for Applied Mathematics, Cornell University, Ithaca, New York 14853, USA*

(Received 24 June 2008; accepted 26 February 2009; published online 27 March 2009; publisher error corrected 1 April 2009)

An inviscid spherical liquid drop held by surface tension exhibits linear oscillations of a characteristic frequency and mode shape (Rayleigh oscillations). If the drop is pinned on a circle of contact the mode shapes change and the frequencies are shifted. The linear problem of inviscid, axisymmetric, volume-preserving oscillations of a liquid drop constrained by pinning along a latitude is solved here. The formulation gives rise to an integrodifferential boundary value problem, similar to that for Rayleigh oscillations, and for oscillations of a drop in contact with a spherical bowl [M. Strani and F. Sabetta, J. Fluid Mech. **141**, 233 (1984)], only more constrained. A spectral method delivers a truncated solution to the eigenvalue problem. A numerical routine has been used to generate the eigenfrequencies/eigenmodes as a function of the location of the pinned circle of constraint. The effect of pinning the drop is to introduce a new low-frequency eigenmode. The center-of-mass motion, important in application, is partitioned among all the eigenmodes but the low-frequency mode is its principal carrier. © *2009 American Institute of Physics*.
[DOI: 10.1063/1.3103344]

I. INTRODUCTION

It is well known that a plucked liquid drop will oscillate, reflecting a competition between inertia and surface tension (capillary action). The study of small, inviscid, free oscillations of an isolated, spherical drop is attributed to Rayleigh.[1] The Rayleigh frequencies of a drop immersed in a second fluid are given by

$$\omega_n^2 = \frac{n(n-1)(n+1)(n+2)}{(n+1)\rho_i + n\rho_e}\frac{\sigma}{R^3}, \tag{1}$$

where σ, ρ_i, ρ_e, and R are surface tension, drop density (interior), density of fluid of immersion (exterior), and the radius of the undeformed drop, respectively. The Rayleigh mode shapes are given by the Legendre polynomials.[2] The $n=0$ and $n=1$ modes are zero frequency modes which can be attributed to conservation of volume and translational invariance, respectively. In practice, the smallest nonzero frequency mode is important, because this mode is typically the first to be excited. The lowest nonzero mode corresponds to $n=2$ for Rayleigh oscillations. Interested in low-gravity applications, Trinh and Wang[3] experimentally verified Eq. (1). These results, which are valid for small perturbations, have been extended to moderate amplitude oscillations by Tsamopoulos and Brown.[4] They use domain constrained perturbations and a Poincaré–Lindstedt expansion to report corrections to both mode shape and frequency at second order in amplitude for both droplets and bubbles.

Viscous effects have also been considered for free oscillations of immiscible drops. Miller and Scriven[5] derived a general dispersion equation for the complex oscillation frequency of a viscous fluid droplet immersed in another viscous fluid for both free and inextensible interfaces, valid for small perturbations. Prosperetti[6] used a normal mode analysis for free interfaces, proposed by Miller and Scriven, to compute the continuous spectrum of a viscous drop in an immiscible liquid. Basaran[7] used a finite element method to numerically investigate the nonlinear oscillations of viscous drops and reports strong mode coupling with finite viscosity and decreased frequency of oscillations for large-amplitude disturbances, along with recovering the linear predictions of Prosperetti.

More recently, attention has been paid to spherical fluid drops under a variety of constraints, because of applications such as inkjet printing, crystal growth and light focusing using liquid lenses.[8–10] Strani and Sabetta considered the linear oscillations of a drop in partial contact with a spherical bowl for both the inviscid[11] and viscous[12] cases. The unperturbed shape is a single spherical drop resting on a spherical support, similar to the contact a golf ball makes with a tee. They found that an additional low-frequency vibrational mode was present ($n=1$), in comparison with isolated drops where it is zero [Eq. (1)]. This low-frequency mode has been attributed to oscillatory motion of the center of mass which arises due to breaking of the translational invariance of the drop. More recent works report observations of center-of-mass motion of constrained drops. Basaran and DePaoli[13] reported oscillatory center-of-mass motion of pendant drops and Bian *et al.*[14] also reported a low-frequency slosh mode for a fluid constrained to a cylindrical tube. In addition, Courty *et al.*[15] showed that the "translational" mode is important for contact times of bouncing spherical droplets. For all these, the free surface is a simply connected domain.

Theisen *et al.*[16] considered a liquid overfilling a small

a)Electronic mail: jbb47@cornell.edu.
b)Electronic mail: phs7@cornell.edu.

cylindrical hole, drilled in a flat plate, in such a way that a droplet protrudes on either side of the plate. The total liquid volume can be adjusted. The top droplet is subjected to air-pressure disturbances from a loudspeaker. Theisen *et al.* modeled the system as spherical-cap drops coupled through a length L of liquid and predict the center-of-mass motion. They compared the predicted frequencies for small-amplitude motions against experiment. The agreement is reasonable. For large-amplitude initial deformations, however, nonspherical shapes are common and the model breaks down. The model in this paper predicts such higher modes and may be expected to be relevant to the experiments in the limit $L \to 0$ (see Sec. V). The droplet-droplet configuration is important to various applications. In *grab-and-release* applications, liquid is pumped into the small droplet to form a liquid bridge against a substrate (grab) and then withdrawn from the droplet to break from the substrate (release).[17] In spherical-cap liquid lens applications, the focal length (radius of curvature) of the liquid lens can be quickly and continuously varied for use in an optical microlens device.[8,9,18,19]

In addition to natural oscillations, there has been extensive research on forced oscillations of constrained drops. For example, Lyubimov *et al.*[20,21] analyzed free and forced oscillations of hemispherical drops for both axisymmetric and nonaxisymmetric cases. DePaoli *et al.*[22] experimentally observed hysteresis phenomenon in large-amplitude forced oscillations of pendant drops, which was numerically observed by Wilkes and Basaran.[23] In another application area, Smith and co-workers[24–26] focused on high-frequency forced oscillations of sessile drops for atomization purposes and low-frequency forced oscillations for droplet ejection. Drop ejection for pendant drops had also been studied by Wilkes and Basaran.[27]

The purpose of this study is to examine the natural axisymmetric oscillations of a liquid drop, pinned on a circle of contact. This work is an extension of the inviscid study of Strani and Sabetta,[11] where the key difference is that the domain of the free surface has two components rather than a single component. The problem may be reduced to solving an integrodifferential boundary value problem on the free surface deformation. The resulting operator equation is identical to that of Rayleigh and of Strani and Sabetta. The respective problems differ only by the boundary conditions which must be enforced.

When considering the oscillations of an isolated fluid drop (Rayleigh), the relevant boundary conditions on the free surface deformation are boundedness of perturbations at the north and south poles ($\theta=0,\pi$). In the Strani and Sabetta problem, the interface deflection must vanish on the bowl of contact in addition to requiring boundedness at the north pole ($\theta=0$). In both cases, the resulting problems are well-posed two-point boundary value problems.

In our problem, pinning the fluid drop on a circle of contact gives rise to an additional boundary condition on the free surface perturbation. This condition, in addition to the boundedness at the poles, defines a three point boundary value problem, thus making the problem overdetermined unlike standard two-point boundary value problems. Strani and Sabetta use a Green's function approach and Legendre series expansions to reduce the problem to an infinite set of algebraic equations.

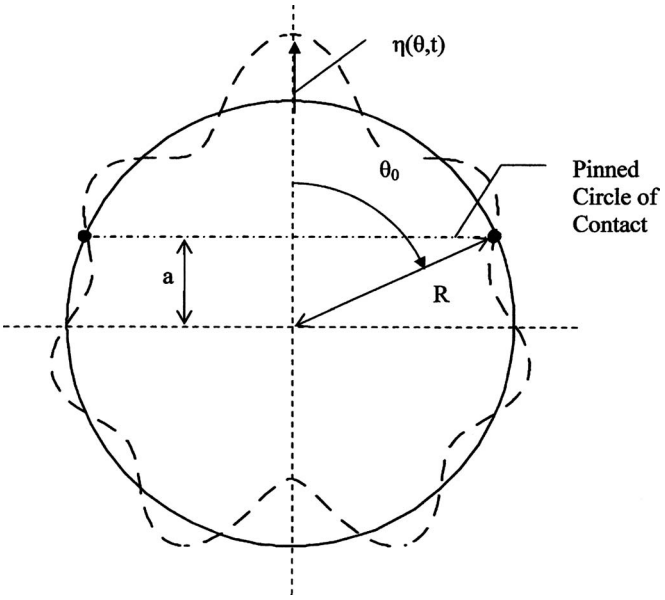

FIG. 1. Definition sketch.

A spectral method is used here to solve the three point integrodifferential boundary value problem. The spherical symmetry of the problem suggests that all relevant quantities (velocity potential, perturbation amplitude) may be expanded using Legendre polynomials, the eigenfunctions that correspond to eigenfrequencies (1). Judicious choice of linear combinations of Legendre polynomials allows one to generate basis functions and thereby a function space which obeys all boundary and integral conditions. A series solution is constructed in this function space and then used to reduce the integrodifferential equation to matrix form, using the standard L_2 inner product.

The pinned circle-of-contact constraint introduces the low-frequency center-of-mass mode, as well as modifies the higher frequency modes, according to the position of the constraint. In general, the higher order mode shapes have an associated center-of-mass motion. That is, the center-of-mass motion partitions predominantly to but not solely to the lowest-frequency mode. Higher mode shapes carry part of the center-of-mass motion and the fraction carried depends on the position of the constraint.

II. MATHEMATICAL FORMULATION

The undisturbed shape of the drop is a sphere of radius R, which is pinned on a latitudinal circle specified by θ_0, as in the definition sketch (Fig. 1). The inner and outer fluids are inviscid and incompressible, the time dependent (time t) free surface deformations $\eta(\theta,t)$ are small and the flow is assumed to be irrotational. The effect of gravity is neglected and only axisymmetric perturbations are considered.

A. Velocity potential

Assuming the flow is irrotational, the velocity field may be written as $\mathbf{v}=-\nabla\phi$, where the velocity potential ϕ satisfies Laplace's equation on the domain, written in a spherical coordinate system as

$$\nabla^2\phi = \sin\theta\frac{\partial}{\partial r}\left(r^2\frac{\partial\phi}{\partial r}\right)+\frac{\partial}{\partial\theta}\left(\sin\theta\frac{\partial\phi}{\partial\theta}\right)=0. \tag{2}$$

The domain is the combined region internal to and external to the droplet, $D\equiv D^i\cup D^e$ where, for linear problems, no domain perturbation is needed,

$$\begin{aligned} D^i &\equiv \{(r,\theta)|0\le r\le R, 0\le\theta\le\pi\},\\ D^e &\equiv \{(r,\theta)|R\le r\le\infty, 0\le\theta\le\pi\}. \end{aligned} \tag{3}$$

B. Pressure

The pressure of the fluid is defined by the linearized Bernoulli equation, valid for small oscillations,

$$p = p_0+\rho\frac{\partial\phi}{\partial t}, \tag{4}$$

over the domain D. This equation applies in both subdomains. When we need to distinguish between subdomains below, we will use superscripts for field quantities and subscripts for material properties. Hence, ρ_i and ρ_e will represent the density of the internal and external fluids, respectively, while p^i and p^e are the internal and external pressures, and so forth.

C. Kinematics

The linearized kinematic condition on the free part of the surface domain ∂D^f relates the radial velocity to the surface deflection there,

$$\frac{\partial\phi}{\partial r}=-\frac{\partial\eta}{\partial t} \quad \text{on} \quad \partial D^f=\{(r,\theta)|r=R,\theta\neq\theta_0\}. \tag{5}$$

At the pinned circle-of-contact ∂D^s, the no penetration condition requires the radial velocity to vanish,

$$\frac{\partial\phi}{\partial r}=-\frac{\partial\eta}{\partial t}=0 \quad \text{on} \quad \partial D^s=\{(r,\theta)|r=R,\theta=\theta_0\}. \tag{6}$$

D. Momentum balance across interface

The normal stress boundary condition for inviscid fluids is written as[28]

$$p^i-p^e=\sigma\nabla\cdot\hat{n}.$$

That is, the pressure difference across the interface is balanced by the surface tension times the curvature of the perturbed interface. For small deflection η, the mean curvature evaluates to the term in the square brackets,

$$p^i-p^e=\sigma\left\{\frac{2}{R}-\frac{1}{R^2}\left[\frac{1}{\sin\theta}\frac{\partial}{\partial\theta}\left(\sin\theta\frac{\partial\eta}{\partial\theta}\right)+2\eta\right]\right\}, \tag{7}$$

which holds on the free part of the interface ∂D^f.

E. Conservation of mass

The surface perturbation is constrained by the constant volume condition (incompressibility),

$$\int_0^\pi \eta\sin\theta d\theta=0. \tag{8}$$

III. REDUCED SYSTEM

The mathematical model may be reduced in the standard way by the use of normal modes,

$$\phi(r,\theta,t)=\xi(r,\theta)e^{i\omega t}, \tag{9}$$

$$\eta(\theta,t)=iy(\theta)e^{i\omega t}, \tag{10}$$

where the deflection is taken $\pi/2$ out of phase with the radial component of velocity (10), consistent with the kinematic condition (5). Substitution of the normal modes (9) and (10) into the governing equations (2)–(8) gives a reduced problem on the new functions ξ and y,

$$\nabla^2\xi=0 \quad \text{on} \quad D, \tag{11}$$

$$\omega(\rho_i\xi^i-\rho_e\xi^e)=-\frac{\sigma}{R^2}\left[\frac{1}{\sin\theta}\frac{\partial}{\partial\theta}\left(\sin\theta\frac{\partial y}{\partial\theta}\right)+2y\right] \quad \text{on} \quad \partial D^f, \tag{12}$$

$$\frac{d\xi}{dr}=\omega y \quad \text{on} \quad \partial D^f, \tag{13}$$

$$\frac{d\xi}{dr}=\omega y=0 \quad \text{on} \quad \partial D^s, \tag{14}$$

$$\int_0^\pi y\sin\theta d\theta=0. \tag{15}$$

Equations (11)–(15) define an eigenvalue problem on the allowable perturbations.

A. Velocity potential solution

The reduced velocity potential ξ obeys Laplace's equation on the domain; Eqs. (11) and (13) may be recognized as a standard Neumann type boundary value problem. Introducing $\mu=\cos\theta$, separation of variables and the method of Frobenius may be used to find a standard solution,

$$\xi^i(r,\mu)=\omega R\left(\xi_0+\sum_{k=1}^{\infty}\frac{\xi_k}{k}\frac{r^k}{R^k}P_k(\mu)\right), \tag{16}$$

$$\xi^e(r,\mu)=-\omega R\left(\sum_{k=1}^{\infty}\frac{\xi_k}{k+1}\frac{R^{k+1}}{r^{k+1}}P_k(\mu)\right), \tag{17}$$

where

$$\xi_k=\frac{(y,P_k)}{(P_k,P_k)},$$

$$(P_k,P_k)=\frac{2}{2k+1}.$$

Here (f,g) is the standard inner product of square integrable functions on the domain $\mu\in(-1,1)$,

$$(f,g)=\int_{-1}^{1}f(\mu)g(\mu)d\mu. \tag{18}$$

B. Surface deformation

Expanding (12) using the new coordinate μ gives

$$\frac{d}{d\mu}\left((1-\mu^2)\frac{dy}{d\mu}\right)+2y = -\frac{\rho_i\omega R^2}{\sigma}\left[\xi^i(R,\mu)-\frac{\rho_e}{\rho_i}\xi^e(R,\mu)\right].$$

The solutions (16) and (17) may be used to reduce the inhomogeneous differential equation on the free surface perturbation, to an integrodifferential equation,

$$(1-\mu^2)\frac{d^2y}{d\mu^2}-2\mu\frac{dy}{d\mu}+2y = -\lambda\left[(y,P_0)+\sum_{k=1}^{\infty}\left(\frac{1}{k}+\frac{\rho_e}{\rho_i}\frac{1}{k+1}\right)\frac{(y,P_k)}{(P_k,P_k)}P_k\right], \tag{19}$$

where $\lambda=\rho_i\omega^2R^3/\sigma$ is the scaled eigenfrequency.

Solutions of Eq. (19) must satisfy the following boundary conditions. All solutions must be bounded at the north and south poles

$$y(\pm1)-\text{bounded}. \tag{20}$$

The no penetration condition (14) reduces to a zero amplitude perturbation condition at the circle of contact, where $a\equiv\cos\theta_0$,

$$y(a)=0. \tag{21}$$

In addition, Eq. (15) reduces to

$$\int_{-1}^{1}y(\mu)d\mu=0. \tag{22}$$

Equations (19)–(22) represent the reduced eigenvalue problem on the free surface perturbation.

IV. SOLUTION METHOD

It is productive to frame the integrodifferential equation as an operator equation,

$$L[y]+\lambda M[y]=0. \tag{23}$$

The linear operators defined via Eq. (19) are

$$L[\bullet]\equiv(1-\mu^2)\frac{d^2}{d\mu^2}\bullet-2\mu\frac{d}{d\mu}\bullet+2\bullet \tag{24}$$

and

$$M\left[\bullet,\frac{\rho_e}{\rho_i}\right]\equiv(\bullet,P_0)+\sum_{k=1}^{\infty}\left(\frac{1}{k}+\frac{\rho_e}{\rho_i}\frac{1}{k+1}\right)\frac{(\bullet,P_k)}{(P_k,P_k)}P_k. \tag{25}$$

Here ρ_e/ρ_i is the density ratio and may be treated as a parameter. If the functions y are restricted to boundary condition (20) and the volume constraint (22), then the eigenvalue problem corresponds to the classical Rayleigh problem. The operators L and M are then self-adjoint and M is a positive operator. Solution gives Legendre polynomials as eigenfunctions, which are the Rayleigh modes, and eigenvalues which correspond to frequencies (1).

Alternatively, the problem may be posed as a variational one following a standard Rayleigh–Ritz procedure. Our strategy will be to construct a function space that incorporates the additional boundary condition (21) and then seek a series solution to Eq. (23) using appropriately chosen basis functions that span this new space.

A. Basis functions

The idea is to construct basis functions $h_k(\mu)$ satisfying Eqs. (20)–(22). Then a solution of the following form is sought:

$$y(\mu)=\sum_{k=1}^{\infty}f_kh_k(\mu). \tag{26}$$

The procedure is straightforward but we offer some details of the steps involved.

To construct the function space, we begin by assuming a test function of the form $g(\mu)=\Sigma_{i=0}^{N}c_iP_i(\mu)$. The Legendre polynomials are used because they form a complete, orthonormal set on the domain[29] and they automatically satisfy Eq. (20).

Consider condition (22) first. Substitute the test function $g(\mu)$ into Eq. (22),

$$\int_{-1}^{1}g(\mu)d\mu=c_0\int_{-1}^{1}P_0(\mu)d\mu+c_1\int_{-1}^{1}P_1(\mu)d\mu+\cdots+c_N\int_{-1}^{1}P_N(\mu)d\mu=0. \tag{27}$$

Since $\int_{-1}^{1}P_i(\mu)d\mu=0$ for all $i\neq0$,[29] the only contribution from Eq. (27) is the first term and $c_0=0$ is determined.

Next, enforcing condition (21) requires

$$g(a)=c_1P_1(a)+c_2P_2(a)+\cdots+c_NP_N(a)=0. \tag{28}$$

This equation can be interpreted as the inner product between a fixed vector and the unknown coefficient vector $[c_1,c_2,\ldots c_N]$. It says that there are $N-1$ linearly independent coefficient N-dimensional vectors that solve Eq. (28). In other words, there are $N-1$ basis functions. They are written as

$$v_k(\mu)=P_k(\mu)-\frac{P_k(a)}{P_1(a)}P_1(\mu),\quad k=2,3,\cdots,N. \tag{29}$$

It can be readily verified that these functions satisfy Eqs. (20)–(22). By the above remark, $N-1$ such functions will span the reduced space (space with constraint incorporated)

or, alternatively, if one function in the direction of the constraint is appended, these N functions will span the original unconstrained space.

The basis functions (29) are linearly independent but they are not orthonormal. For efficiency in computations, it is convenient to work with an orthonormal set. The last step is to use a Gram–Schmidt procedure on v_k to deliver orthonormal functions, h_k, renumbered $k=1,2,\cdots,N-1$. This step is done using symbolic computer algebra.

B. Reduction to matrix form

We start by writing the truncated expansion,

$$y(\mu)=\sum_{k=1}^{N-1} f_k h_k(\mu). \tag{30}$$

Note that this is an order $N-1$ approximation in the reduced space but an order N approximation in the unconstrained space. That is, the surface perturbation has $N-1$ degrees of freedom, all orthogonal to the constraint direction (the Nth dimension). The operator equation (23) is reduced to a matrix equation

$$T_{ij}f_j=0 \tag{31}$$

by taking inner products with the basis functions,

$$T_{ij}=(L[h_i]+\lambda M[h_i],h_j)=\int_{-1}^{1}(L[h_i]+\lambda M[h_i])h_j d\mu. \tag{32}$$

For example, the $1j$ position is the projection onto the jth basis function, when the operator is applied to the first basis function.

Solutions of Eq. (31) determine the eigenvalues λ_n and the eigenvectors $\hat{f}^{(n)}$. The eigenfunctions y_n are then constructed by applying the eigenvector coefficients $\hat{f}_k^{(n)}$ to the orthonormal basis functions h_k,

$$y_n(\mu)=\sum_{k=1}^{N-1}\hat{f}_k^{(n)}h_k(\mu). \tag{33}$$

The eigenfunctions are determined only up to a constant and the final step is to fix that constant by specifying,

$$\hat{y}_n=\frac{y_n}{\max(|y_n(-1)|,|y_n(1)|)}. \tag{34}$$

This scaling is reminiscent of the Rayleigh eigenfunctions where a similar scaling is applied to the north pole only ($\mu=1$). We scale with respect to the maximum displacement at either pole ($\mu=\pm 1$) because, unlike the Legendre polynomials (Rayleigh eigenfunctions), our eigenfunctions are neither symmetric nor antisymmetric about the equator and because the norm on the eigenfunctions is inherited from the norm on the Legendre polynomials.

A number of checks on the computational results are performed. Limiting cases can be compared to results in literature and these will be discussed in Sec. V. Another check uses the self-adjoint nature of the operator L. The null space of L is found to be $P_1(\mu)$, which has a node at $a=0$, thus

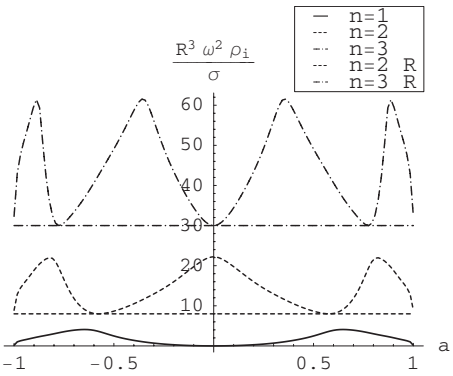

FIG. 2. Eigenfrequency vs pin location ($\rho_e/\rho_i=0$).

satisfying Eq. (21). The Fredholm alternative applied to Eq. (23) requires that the right hand side, $\lambda M[y]$, be orthogonal to the null space of L; that is,

$$[P_1(\mu),-\lambda M(h_j)]=0, \tag{35}$$

where

$$M(h_j)\equiv\sum_{k=1}^{\infty}\left(\frac{1}{k}+\frac{\rho_e}{\rho_i}\frac{1}{k+1}\right)\left[\frac{(h_j(\mu),P_k(\mu))}{(P_k(\mu),P_k(\mu))}\right]P_k(\mu).$$

The term in the brackets on the right hand side is nonzero, which requires that $\lambda=0$. The computational results show that the $n=1$ eigenfrequency tends to zero when the circle of contact tends to the equator of the fluid drop ($a=0$), consistent with the Fredholm alternative requirement.

V. RESULTS

The modes and vibration frequencies of the constrained fluid drop are computed. The scaled frequencies λ_n for the first three modes are plotted in Fig. 2 as a function of the location of the circle of contact a, for $\rho_e/\rho_i=0$. Also plotted, as horizontal lines, are the corresponding Rayleigh frequencies (R in the legend). The frequency of the constrained problem is never lower than that of the unconstrained problem, with equality achieved whenever the constraint falls on a node of the corresponding Rayleigh mode (i.e., a node of a Legendre polynomial). This is anticipated since the constraint is satisfied "naturally" in the latter case. What is not anticipated is that the constrained frequency can more than double the Rayleigh frequency for certain pin locations. For example, pinning the $n=2$ mode at the equator raises the frequency from 8 to 22.

Much like the local minimums of Fig. 2 which occur at "natural" pin locations, the local maximums occur at "unnatural" pin locations with respect to the "unconstrained" Rayleigh modes. The definition of an "unnatural" pin location becomes apparent when the eigenfrequencies and eigenmodes are computed. The results presented here were obtained with a 13 term expansion, which gives convergence of the first three eigenfrequencies to within 0.1% for all pin locations. The rate of convergence depends upon the pin location. For example, the $n=2$ mode shows convergence to the prescribed tolerance (0.1%) using only five terms for $a=-0.557$, a natural location for this mode. On the other

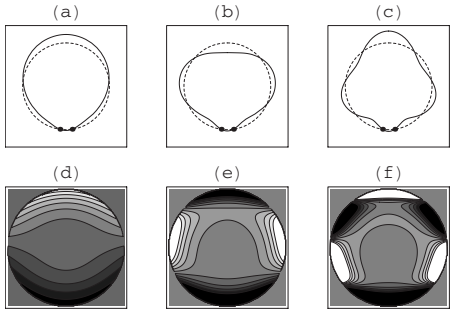

FIG. 3. Eigenmode [(a)–(c)] and velocity potential [(d)–(f)] for $a=-0.99$. Mode $n=1$ [(a) and (d)], $n=2$ [(b) and (e)], and $n=3$ [(c) and (f)].

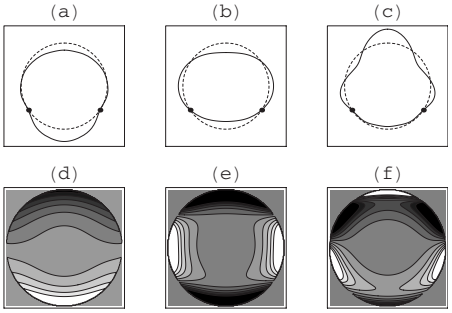

FIG. 5. Eigenmode [(a)–(c)] and velocity potential [(d)–(f)] for $a=-0.557$. Mode $n=1$ [(a) and (d)], $n=2$ [(b) and (e)], and $n=3$ [(c) and (f)].

hand, if the drop is pinned at the equator, the $n=2$ mode converges to the prescribed tolerance using 10 terms. If one desires the eigenfrequency and mode shape for a high wavenumber, say $n=20$, the number of terms necessary in the expansion is of the order 30. However, the recursive nature of the Gram–Schmidt procedure makes it very computationally intensive to generate 30 orthonormal basis functions; this is the step that computationally limits the approach.

Figure 2 also shows that pinning the drop introduces a low-frequency mode $(n=1)$ not present in the Rayleigh case. This mode has been reported previously by Strani and Sabetta,[11] among others. The Strani study considered a drop in partial contact with a spherical-cap support, remarking that the new mode "tends to a zero frequency rigid displacement" as the constrained portion of the surface vanishes. The Strani limit of the contact region shrinking to a point $(\theta\rightarrow\pi)$ coincides with our limit of the circle shrinking to a pole $(a\rightarrow\pm1)$. Our results agree with Strani's in this common limit and both results tend to the corresponding frequencies (1). Mode shapes and velocity potentials for this case are shown in Fig. 3.

Another special pinning location is the equator. For the Rayleigh problem, all odd modes have a node at $\mu=0$. Therefore, when $a=0$, all odd constrained frequencies correspond to odd Rayleigh frequencies. The mode shapes are shown in Fig. 4, above the corresponding velocity potentials, where $P_1(\mu)$ and $P_3(\mu)$ are recognized as shapes for $n=1$ and $n=3$. Figure 5 shows the first three eigenfunctions for $a=-0.557$, which is the location of a node for $P_2(\mu)$. Not surprisingly, the second mode shape corresponds to $P_2(\mu)$.

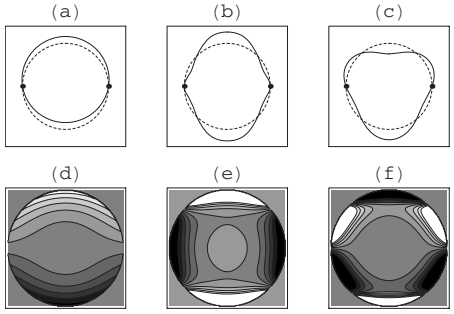

FIG. 4. Eigenmode [(a)–(c)] and velocity potential [(d)–(f)] for $a=0$. Mode $n=1$ [(a) and (d)], $n=2$ [(b) and (e)], and $n=3$ [(c) and (f)].

In view of the completeness of the Legendre polynomials, any shape can be decomposed into a weighted sum of $P_n(\mu)$. These weights, for the mode shapes shown in Figs. 3–5 are reported in Appendix B for reference.

For the Rayleigh problem, the $n=1$ mode has zero frequency (1) and may be associated with the linearized center-of-mass motion of the drop (see Appendix A). The imposed constraint, fixed in the laboratory frame, breaks the translational invariance to typically yield a nonzero frequency for the center-of-mass motion. For the Rayleigh modes, the center-of-mass motion is completely determined by the $n=1$ mode and the higher order mode shapes are effectively decoupled for motion of the center of mass. In contrast, there is no such simple partition for constrained motions.

Our interest is in what role the center of mass plays in the higher modes that we report in this paper. To that end, the contribution of the center of mass motion (z_{cm}) to any mode is found to be $(z_{\mathrm{cm}})/R=3/2ie^{i\omega_n t}(\hat{y}_n,P_1)$ in Appendix A. Understanding this contribution is important in applications such as ink-jet printing where generating large excursions of the center-of-mass often correlates with pinch-off of droplets. Even though this paper restricts to small-amplitude motions, such linear results are known to often carry through to nonlinear behavior.

The center of mass is found to oscillate at the eigenfrequency ω_n with a contribution to the eigenmode $(\hat{y}_n,P_1)$. Figure 6 shows the decomposition $(z_{\mathrm{cm}})_n=(\hat{y}_n,P_1)$ as a function of pinning location. The $n=1$ mode carries the majority of the center-of-mass motion, but not all of it. The higher mode shapes are accompanied by an associated motion of the center of mass, thereby coupling the translation and oscillatory Rayleigh modes. Richard *et al.*[30] postulated that this

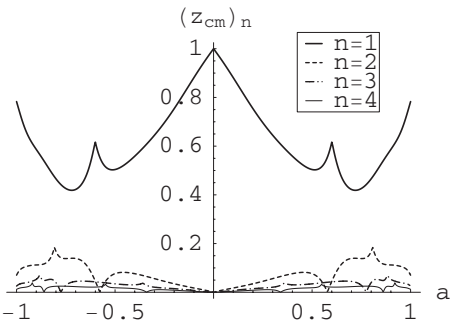

FIG. 6. Center-of-mass motion contribution to eigenmodes

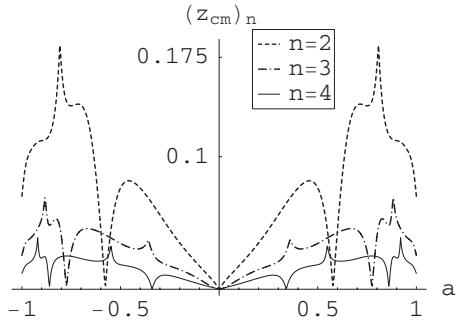

FIG. 7. Center-of-mass motion contribution to higher eigenmodes (blowup of Fig. 6)

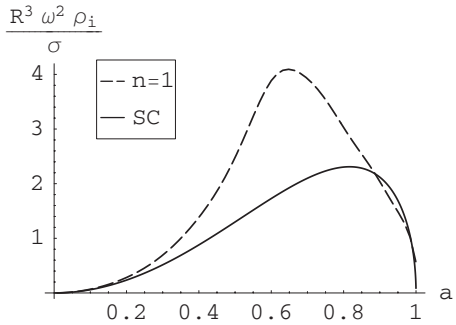

FIG. 9. Frequency vs pin location: spherical-cap (SC) and $n=1$ mode.

coupling might explain the discrepancy between experimental and theoretical prefactor values for contact and impact times for droplet bouncing.[15] While it may be convenient to think of the $n=1$ mode as a center-of-mass mode, it is clearly an approximation, at best.

The ordering of the center-of-mass decomposition for the $n>1$ modes is not preserved with pin location (Fig. 7). For example, the $n=2$ mode carries less center-of-mass motion than the $n=3$ or $n=4$ mode for a pin location near $a=0.557$ [the node of $P_2(\mu)$].

For a fixed initial deformation amplitude and/or kinetic energy, suppose one would like to excite a preferred mode to get the greatest extension of the center of mass in order to encourage a pinch-off of a certain volume, say, Figs. 6 and 7 provide a guide as how to choose the optimal pin location for such behavior.

The above results have illustrated the behavior for $\rho_e=0$. Results for other density ratios are readily computed. Increasing the ratio of outer to inner density (ρ_e/ρ_i) is found to decrease the eigenfrequencies compared to the case of an isolated fluid drop $(\rho_e=0)$. Let λ_n^0 denote the nth eigenfrequency for $\rho_e=0$ and λ_n be the eigenfrequency for $\rho_e\neq 0$. Using the definition of λ, we set $\Omega^2=\lambda_n^0/\lambda_n$ as the ratio of the eigenfrequency for an isolated drop to the eigenfrequency for $\rho_e\neq 0$. The computed Ω^2 against (ρ_e/ρ_i) is shown in Fig. 8. It is seen that a nonzero outer density has a greater effect on the higher frequency modes, which is consistent with the numerical results of Strani and Sabetta for varying density ratios in the common limit, $a\to -1$ (Fig. 8).

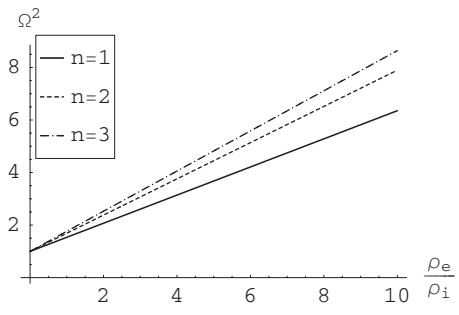

FIG. 8. Density variation in eigenmodes for $a=-0.99$.

VI. CONCLUDING REMARKS

The classical Rayleigh problem can be posed as a variational problem for a quadratic functional. The minimization is taken over functions that satisfy conditions (20) and (22). We refer to this as the unconstrained problem. Equation (23) represents the corresponding Euler–Lagrange equation, obtained by requiring the first variation to vanish. In this paper, as an extension of the Rayleigh problem, we have restricted candidate functions to be pinned on a latitudinal circle-of-constraint (21). Using the Rayleigh–Ritz variational approach,[31] one can show that the frequency of the constrained problem cannot decrease relative to the unconstrained one. The eigenvalues and eigenfunctions of the constrained problem that we compute directly are consistent with these bounds.

One motivation for our study is to compare against predictions of the spherical-cap model. Theisen *et al.*[16] restricted to spherical-cap shapes in considering the dynamics of the center of mass of two droplets coupled through a tube. In the limit of zero tube length, the system reduces to two spherical caps coupled along a common circle-of-contact. When the two caps are complementary pieces of a sphere, the equilibrium state corresponds to a sphere with a latitudinal circle-of-constraint, the problem that we consider. Among other results, they report frequency of oscillation of small-amplitude motions as it depends on a. The frequency of our mode $n=1$ shows a qualitatively similar dependence on a as the spherical-cap mode (Fig. 9). Both give an oscillation frequency of zero when $a=0$ and $a=1$ and have a single maximum near $a=0.7$. On the other hand, there is quantitative discrepancy between the frequencies. This can be traced to the different shapes allowed near the circle of constraint. For the spherical caps, the tangent to the interface from below and from above the pinning latitude must be discontinuous (except for equilibrium shapes). On the other hand, the formulation in this paper does not allow a singularity in curvature, which precludes discontinuous slopes. Thus, the spherical-cap shape may reasonably capture the observed frequencies for finite nonzero tube lengths but will likely fail quantitatively for sufficiently short tubes.

The issues are illustrated in Fig. 10. A snapshot of the two coupled drops, digitally modified to remove the tube, is seen in Fig. 10(a)[16] Figure 10(b) shows the $n=2$ computed eigenmode, for a pin location slightly away from the equator to account for small gravitational effects on the static equi-

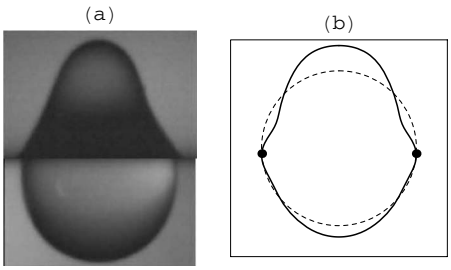

FIG. 10. Comparison of (a) experiment against (b) predicted $n=2$ eigenmode for $a=0.05$.

librium shape. This qualitative comparison is acceptable if one ignores the behavior near the contact line. The photograph shows different apparent contact angles for the top and bottom interfaces, a feature especially apparent at the right side where the top contact line has evidently depinned. Furthermore, comparison near the contact-line, photo against computation, shows a different curvature. In addition, it should be noted that in the computed shape, the tangents at the contact-line appear dissimilar at this scale but are actually smooth, consistent with the discussion of the previous paragraph. Because of the contact-line issues and the influence of the tube, quantitative comparison with the experiments is precluded. The point here is to elucidate these issues.

A practical question regarding the computations presented in this paper is whether there is a preferred way to excite the system to get the greatest extension of the center of mass, say, for a fixed constraint position and initial deformation amplitude. Clearly, the $n=1$ mode carries the majority of the center-of-mass motion, but the excursion of the $n=2,3,\ldots$ modes may be unexpected. One might think that the lower order modes to carry more of the center of mass than the higher order modes, considering that the velocity fields for the higher order modes are more localized on the surface (see Sec. II A). On the contrary, for certain pin locations, it is seen that the higher modes carry more of the center-of-mass motion. For these pin locations, to get the greatest extension of the center of mass, one should preferentially excite particular modes.

A goal of this work is to extend Strani and Sabetta's analysis to include "belts" of restricted deformation on the sphere. That is, suppose one wishes to pin the interface between north latitudes 50° and 70°. This can be done by adding a number of circular pinning constraints. Appendix C shows how the analysis for a single constraint can be readily generalized to two pinned circles. The spherical bowl constraint considered by Strani is recovered with a sufficient number of closely placed pinning circles. A result of the analysis for two circles is that the frequency gaps seen in Fig. 2 begin to fill. That is, according to Fig. 2, there is no pinning location to give a scaled frequency between 22 and 30. By adding a second constraint, one can choose a pin location to achieve any desired frequency.

ACKNOWLEDGMENTS

The image from experiment in Fig. 10 was taken from high-speed video recording of oscillation experiments done in the Hirsa Laboratory at RPI (reported in Ref. 16). This work was supported by the NSF under Grant Nos. DMI-0500311 and CBET-0653831, and DARPA.

APPENDIX A: CENTER-OF-MASS MOTION

Here we use the definition of the center of mass to decompose the eigenmodes into center-of-mass motion (Figs. 6 and 7). The center-of-mass resides on the z-axis due to the assumed axisymmetry of perturbations. We may define the center-of-mass z_{cm} of a given perturbation $\eta(\theta,t)$ in the standard way as

$$mz_{\mathrm{cm}} = \int z\,dm = 2\pi\rho\int_0^{\pi}\int_0^{r} r^3\sin(\theta)\cos(\theta)\,dr\,d\theta$$

$$= \frac{\rho\pi}{2}\int_0^{\pi} r^4\sin(\theta)\cos(\theta)\,d\theta, \tag{A1}$$

where the radial perturbation coordinate is defined in Fig. 1 as

$$r = R[1+\epsilon\eta(\theta,t)], \tag{A2}$$

and

$$r^4 = R^4[1+\epsilon\eta(\theta,t)]^4 = R^4\{1+\epsilon[4\eta(\theta,t)]+\cdots\}. \tag{A3}$$

Likewise, the center-of-mass coordinate may be expanded as

$$z_{\mathrm{cm}} = (z_{\mathrm{cm}})_0 + \epsilon(z_{\mathrm{cm}})_1 + \cdots. \tag{A4}$$

Expanding Eq. (A1) in ϵ gives

$$m[(z_{\mathrm{cm}})_0 + \epsilon(z_{\mathrm{cm}})_1 + \cdots]$$

$$= \frac{\rho\pi R^4}{2}\int_0^{\pi}[1+\epsilon 4\eta(\theta,t)+\cdots]\sin(\theta)\cos(\theta)\,d\theta, \tag{A5}$$

$$m[(z_{\mathrm{cm}})_0 + \epsilon(z_{\mathrm{cm}})_1 + \cdots]$$

$$= \frac{\rho\pi R^4}{2}\int_0^{\pi}\sin(\theta)\cos(\theta)\,d\theta + \epsilon 2\pi\rho R^4\int_0^{\pi}\eta(\theta,t)$$

$$\times\sin(\theta)\cos(\theta)\,d\theta + \cdots. \tag{A6}$$

Using $\mu=\cos(\theta)$, $m=\rho\frac{4}{3}\pi R^3$ and equating terms of the same order we find

$$(z_{\mathrm{cm}})_0 = 0, \tag{A7}$$

$$(z_{\mathrm{cm}})_1 = \tfrac{3}{2}R[\eta_n(\mu,t),P_1(\mu)]. \tag{A8}$$

Using the definition of $\eta_n(\mu,t)$ as an eigenmode,

$$\eta_n(\mu,t) = ie^{i\omega_n t}\hat{y}_n(\mu), \tag{A9}$$

the scaled center-of-mass motion is

$$\frac{(z_{\mathrm{cm}})_1}{R} = \frac{3}{2}ie^{i\omega_n t}(\hat{y}_n,P_1). \tag{A10}$$

APPENDIX B: DECOMPOSITION OF EIGENMODES

A given eigenmode $\hat{y}_n(\mu)$ may be decomposed into the Rayleigh modes as follows:

$$\hat{y}_n(\mu) = \sum_{k=1}^{\infty} b_k P_k(\mu), \tag{B1}$$

where

$$b_k = \frac{(\hat{y}_n, P_k)}{(P_k, P_k)} = \frac{2k+1}{2}(\hat{y}_n, P_k). \tag{B2}$$

A numerical routine was run using a 13 term expansion. Shown below is the decomposition of the first four eigenmodes into the first eight coefficients of the 13 term expansion, for the pin locations used to generate Figs. 3–5:

(1) Rayleigh decomposition for $a=-0.99$.

n	b_1	b_2	b_3	b_4	b_5	b_6	b_7	b_8
1	0.784	0.321	−0.160	0.108	−0.080	0.061	−0.048	0.038
2	−0.084	0.804	0.383	−0.188	0.127	−0.095	0.073	−0.057
3	−0.031	0.128	−0.783	−0.453	0.206	−0.136	0.100	−0.076
4	0.015	−0.056	0.152	−0.719	−0.511	0.212	−0.135	0.097

(2) Rayleigh decomposition for $a=0.001$.

n	b_1	b_2	b_3	b_4	b_5	b_6	b_7	b_8
1	0.999	0.001	0	0	0	0	0	0
2	0	0.644	−0.008	0.523	0.002	−0.214	−0.001	0.132
3	0	0.004	0.991	0.006	0	−0.002	0	0.001
4	0	−0.104	0	0.589	−0.028	0.570	0.002	−0.222

(3) Rayleigh decomposition for $a=-0.557$.

n	b_1	b_2	b_3	b_4	b_5	b_6	b_7	b_8
1	0.488	−0.072	0.312	−0.189	0.018	0.084	−0.085	0.023
2	0.034	0.928	0.064	−0.034	0.003	0.014	−0.014	0.004
3	0.039	0.010	−0.619	−0.499	0.028	0.108	−0.101	0.026
4	−0.027	−0.006	0.177	−0.482	−0.476	−0.377	0.269	−0.062

APPENDIX C: BASIS FUNCTIONS FOR A DOUBLE PINNED FLUID DROP

The analysis outlined previously can be extended to the case of a double-pinned spherical fluid drop, where we define a and b as the location of the pinned circles-of-contact. We now augment Eqs. (20)–(22) with a boundary condition on the radial velocity amplitude or equivalently the perturbation amplitude at the second pinned circle-of-contact. Now, the boundary/integral conditions to be satisfied are as follows:

$$y(a) = 0, \tag{C1}$$

$$y(b) = 0, \tag{C2}$$

$$\int_{-1}^{1} y(\mu)d\mu = 0. \tag{C3}$$

By the same reasoning as Sec. IV, we seek to construct basis functions which obey all necessary conditions and use them to form an approximate solution to the integrodifferential operator equation. We begin again by assuming a test function of the form

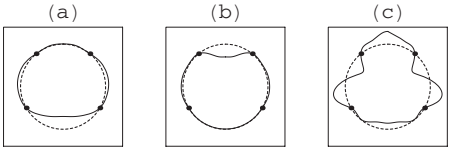

FIG. 11. Eigenmodes for $a=0.775$, $b=-0.5$, (a) first, (b) second, and (c) third modes.

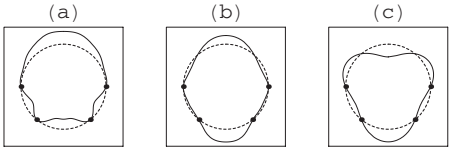

FIG. 12. Eigenmodes for $a=-0.775$, $b=0.001$, (a) first, (b) second, and (c) third modes.

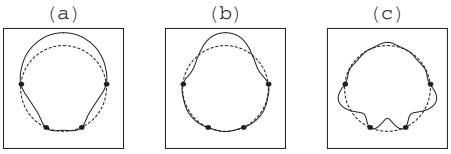

FIG. 13. Eigenmodes for $a=-0.91$, $b=0.1$, (a) first, (b) second, and (c) third modes.

$$g(\mu) = \sum_{i=0}^{N} c_i P_i(\mu). \tag{C4}$$

Equation (C3) requires that $c_0=0$, as was the case for the single pinned circle of contact. Plugging Eq. (C4) into Eqs. (C1) and (C2) gives

$$g(a) = c_1 P_1(a) + c_2 P_2(a) + \cdots + c_N P_N(a), \tag{C5}$$

$$g(b) = c_1 P_1(b) + c_2 P_2(b) + \cdots + c_N P_N(b), \tag{C6}$$

or equivalently,

$$\begin{bmatrix} P_1(a) & P_2(a) & \cdots & P_N(a) \\ P_1(b) & P_2(b) & \cdots & P_N(b) \end{bmatrix} \begin{bmatrix} c_1 \\ c_2 \\ \vdots \\ c_N \end{bmatrix} = [0]. \tag{C7}$$

Some linear algebra on Eq. (C7) allows one to find $N-2$ linearly independent basis functions, which satisfy Eqs. (C1)–(C3),

$$\begin{aligned} v_n(\mu) = P_n(\mu) - \frac{P_n(a)}{P_1(a)} P_1(\mu) \\ - \frac{[P_1(a)P_n(b) - P_n(a)P_1(b)]}{[P_1(a)P_2(b) - P_2(a)P_1(b)]} P_2(\mu) \\ + \frac{P_2(a)}{P_1(a)} \frac{[P_1(a)P_n(b) - P_n(a)P_1(b)]}{[P_1(a)P_2(b) - P_2(a)P_1(b)]} P_1(\mu). \end{aligned} \tag{C8}$$

We again apply the Gram–Schmidt procedure to these linearly independent functions and use them in the operator equation (23) to reduce the problem to a truncated set of algebraic equations. Shown in Figs. 11–13 are a few examples of the eigenfunctions so obtained.

[1] L. Rayleigh, "On the capillary phenomenon of jets," Proc. R. Soc. London **29**, 71 (1879).
[2] H. Lamb, *Hydrodynamics* (Cambridge University Press, Cambridge, UK, 1932).
[3] E. Trinh and T. Wang, "Large-amplitude free and driven drop-shape oscillation: experimental results," J. Fluid Mech. **122**, 315 (1982).
[4] J. Tsamopoulos and R. Brown, "Nonlinear oscillations of inviscid drops and bubbles," J. Fluid Mech. **127**, 519 (1983).
[5] C. Miller and L. Scriven, "The oscillations of a fluid droplet immersed in another fluid," J. Fluid Mech. **32**, 417 (1968).
[6] A. Prosperetti, "Normal-mode analysis for the oscillations of a viscous liquid drop in an immiscible liquid," J. Mec. **19**, 149 (1980).
[7] O. Basaran, "Nonlinear oscillations of viscous liquid drops," J. Fluid Mech. **241**, 169 (1992).
[8] S. Kuiper and B. Hendriks, "Variable-focus liquid lens for miniature cameras," Appl. Phys. Lett. **85**, 1128 (2004).
[9] C. Lopez, C. Lee, and A. Hirsa, "Electrochemically activated adaptive liquid lens," Appl. Phys. Lett. **87**, 134102 (2005).
[10] C. Lopez and A. Hirsa, "Fast focusing using a pinned-contact liquid lens," Nat. Photonics **2**, 610 (2008).
[11] M. Strani and F. Sabetta, "Free vibrations of a drop in partial contact with a solid support," J. Fluid Mech. **141**, 233 (1984).
[12] M. Strani and F. Sabetta, "Viscous oscillations of a supported drop in an immiscible fluid," J. Fluid Mech. **189**, 397 (1988).
[13] O. Basaran and D. DePaoli, "Nonlinear oscillations of pendant drops," Phys. Fluids **6**, 2923 (1994).
[14] X. Bian, M. Perlin, W. Schultz, and M. Agarwal, "Axisymmetric slosh frequencies of a liquid mass in a circular cylinder," Phys. Fluids **15**, 3659 (2003).
[15] S. Courty, G. Lagubeau, and T. Tixier, "Oscillating droplets by decomposition on the spherical harmonic basis," Phys. Rev. E **73**, 045301 (2006).
[16] E. Theisen, M. Vogel, C. Hirsa, A. Lopez, and P. Steen, "Capillary dynamics of coupled spherical-cap droplets," J. Fluid Mech. **580**, 495 (2007).
[17] M. Vogel, P. Ehrhard, and P. Steen, "The electroosmotic droplet switch: Countering capillarity with electrokinetics," Proc. Natl. Acad. Sci. U.S.A. **102**, 11974 (2005).
[18] D. Zhang, V. Lien, Y. Berdichevsky, J. Choi, and Y. Lo, "Fluidic adaptive lens with high focal length tunability," Appl. Phys. Lett. **82**, 3171 (2003).
[19] D. Zhang, N. Justis, and Y. Lo, "Fluidic adaptive lens of transformable lens type," Appl. Phys. Lett. **84**, 4194 (2004).
[20] D. Lyubimov, T. Lyubimova, and S. Shklyaev, "Behavior of a drop on an oscillating solid plate," Phys. Fluids **18**, 012101 (2006).
[21] D. Lyubimov, T. Lyubimova, and S. Shklyaev, "Non-axisymmetric oscillations of a hemispheric drop," Fluid Dyn. **39**, 851 (2004).
[22] W. DePaoli, J. Feng, O. Basaran, and T. Scott, "Hysteresis in forced oscillations of pendant drops," Phys. Fluids **7**, 1181 (1995).
[23] E. Wilkes and O. Basaran, "Hysteretic response of supported drops during forced oscillations," J. Fluid Mech. **393**, 333 (1999).
[24] B. Vukasinovic, M. Smith, and A. Glezer, "Dynamics of a sessile drop in forced vibration," J. Fluid Mech. **587**, 395 (2007).
[25] A. James, B. Vukasinovic, M. Smith, and A. Glezer, "Vibration-induced drop atomization and bursting," J. Fluid Mech. **476**, 1 (2003).
[26] A. James, M. Smith, and A. Glezer, "Vibration-induced drop atomization and the numerical simulation of low-frequency single-droplet ejection," J. Fluid Mech. **476**, 29 (2003).
[27] E. Wilkes and O. Basaran, "Drop ejection from an oscillating rod," J. Colloid Interface Sci. **242**, 180 (2001).
[28] P. Drazin, *Introduction to Hydrodynamic Stability* (Cambridge University Press, Cambridge, UK, 1981).
[29] T. MacRobert, *Spherical Harmonics* (Pergamon, New York, 1967).
[30] D. Richard, C. Clanet, and D. Quere, "Contact time of a bouncing drop," Nature (London) **417**, 811 (2002).
[31] L. Segel, *Mathematics Applied to Continuum Mechanics* (Dover, New York, 1987).